*Journal of Applied Polymer Science*

WILEY

Applied Polymer SCIENCE

RESEARCH ARTICLE OPEN ACCESS

# Processability and Performance of Dual-Cure Resins: A Study of Cyanate Ester Integration for DLP

Max Friedel | Nico Geis | Heiko Stieger | Holger Ruckdaeschel

Department of Polymer Engineering, University of Bayreuth, Bayreuth, Bavaria, Germany

**Correspondence:** Holger Ruckdaeschel (holger.ruckdaeschel@uni-bayreuth.de)

**Received:** 23 April 2025 | **Revised:** 4 July 2025 | **Accepted:** 11 July 2025

**Funding:** This work was supported by Bayerische Staatsministerium für Wirtschaft, Landesentwicklung und Energie (ROB-2-3410.20-04-10/BLU-2109-0010).

**Keywords:** mechanical properties | resins | thermal properties

## ABSTRACT

This study investigates dual-cure resins for the DLP process using photorheological and thermomechanical characterization methods to optimize their mechanical, thermal, and processing properties for resin printing. The focus was on the incorporation of different cyanate esters (CE) as thermally curing components combined with a UV-curing acrylate system to create an interpenetrating network (IPN). The results show that increasing the CE content significantly improves the thermal properties, especially the glass transition temperature ($T_g$) and the thermal stability ($T_{\Delta 5\%}$). However, beyond a CE content of 50 wt.%, the print resolution decreases, as shown by photorheological measurements and printing trials. Photorheology also showed that higher CE concentrations reduce viscosity and improve processability, and mechanical tests confirmed that the developed resin formulations have properties comparable to a commercial system. Among the formulations tested, the system with a CE content of 50%LVT100 stood out, achieving an optimal balance of thermal and mechanical performance while maintaining high print quality on standard DLP printers. This research introduces an open and adaptable high-performance resin formulation that can be used without proprietary printing systems, potentially enabling new applications and fostering competition in the high-performance resin market.

## 1 | Introduction

Additive manufacturing of polymers has made great strides over the last three decades in areas such as biomedicine, art, and engineering [1–4]. Particularly in the engineering sector, after the development of basic printing technologies, the focus has shifted to high-performance materials to enable applications such as automotive or aerospace in all three major material classes (metals, ceramics and polymers) [5–7]. An approach in the field of polymers exists in the most conventional processing method, Fused Filament Fabrication, with the integration of functional particles or fibers, or the processing of high-temperature thermoplastics such as polyetheretherketone (PEEK) [8–11]. Since thermosets typically have better thermomechanical properties than thermoplastics even without reinforcement, there is an increasing effort to use resin systems in high-performance applications, with companies pushing the limits with new printing and resin systems [12]. Fully resin-based parts are rarely used in safety-critical applications due to concerns about the reliability of resin-printed parts. Many of these concerns stem from experiences with fused filament fabrication, where anisotropic material and low thermomechanical properties are a common problem in meeting the stringent regulations of, for example, aerospace certification requirements [13, 14]. In contrast, resin printing offers near-isotropic properties and high

[Correction added on August 25, 2025, after first online publication: Heiko Stieger was included as third author.]

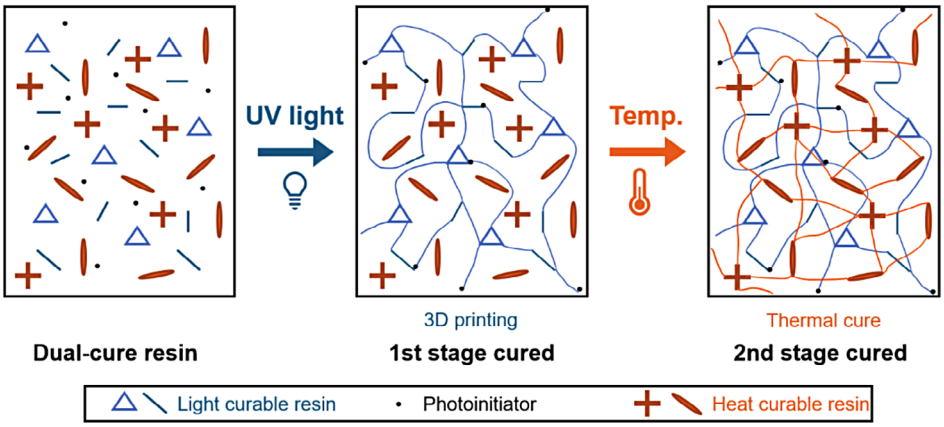


**FIGURE 1** | Schematic step-by-step dual-curing process. [Color figure can be viewed at wileyonlinelibrary.com]

performance [15]. To further reduce skepticism, the industry is developing a new generation of printing resins, dual-cure resins, designed to improve the consistency and reliability of the additive-manufactured components.

These dual-cure resins typically consist of two components: a UV-curable part and a thermally curable part [16]. The UV-curable part is generally comparable to standard resin systems, including monomers, oligomers, reactive diluents, photoinitiators, and other additives, such as pigments or toughening agents, and follows the principle of radical polymerization [17–19]. The thermally curable part consists of epoxy resins (EP), bismaleimides (BMI) or cyanate esters (CE). Catalysts are also used to reduce the curing temperature of the thermal component and to protect the acrylic component from degradation [20–26]. The printing process is therefore divided into two steps: the printing of the green part using SLA or DLP (with UV post-curing) and the thermal curing. Figure 1 shows the steps schematically. The UV exposure in the 3D printer and the post-curing process ensure that the oligomeric and monomeric acrylates are crosslinked by the radical reaction of the photoinitiator. The condition of the samples immediately after 3D printing without UV curing is called green body. At a sufficiently high temperature, the thermally curing components subsequently crosslink with each other [27].

In this process, a sequential IPN is formed. The UV-curing acrylate network develops first, and the thermally formed network polymerizes in situ to the first network [27]. In principle, there are different definitions for IPNs. In this case, we are assuming two networks that are intertwined on the polymer scale but not covalently bonded to each other [27, 28]. The combination of acrylate and thermal curing component can simultaneously improve light-induced and thermal curing. The nonreacting liquid thermal curing component creates a plasticizing effect during UV curing, which increases the conversion rate and speed of acrylate curing. On the other hand, the acrylate component autocatalytically supports thermal curing [29].

Most academic dual-cure resin systems rely on EP for the thermal component. These are widely used and cost effective. However, the disadvantage of EP is that its glass transition temperature ($T_g$) typically does not exceed 200°C, which severely limits high-temperature applications. In combination with the UV-curing component, the thermal properties are further reduced [30]. In order to use dual-cure resins at higher temperatures, efforts are being made to use BMIs and CEs. In terms of price, BMIs and CEs are significantly more expensive than EP, but also have $T_g$ values above 250°C [31]. Studies indicate that a higher amount of thermoset component could improve mechanical and thermal properties, but also has the potential to reduce green strength. The only commercial dual-cure resin with the use of CE, CE-221 from Carbon, has a glass transition temperature of 220°C, high chemical resistance, and excellent UV stability [26, 32, 33].

The purpose of this work is to improve the understanding of how dual-cure formulations with different cyanate esters affect key resin printing parameters by also using the emerging method of photorheology. We are also investigating the thermomechanical behavior and limitations of these dual-cure resins. In addition, we hope to facilitate access to dual-cure resins with a final formulation applicable to any standard resin printer, which can be seen as a new starting point in resin development to enhance stimulating competition in the currently narrow high-performance resin printing market.

## 2 | Experimental

### 2.1 | Materials

For this work, we varied the amount and type of CE, which required a constant UV-curable system. For this reason, an in-house-developed high-performance acrylate system was used to ensure as close a match as possible to the CE, which will be further referred to as AY, standing for acrylate part.

For AY, Tricyclodecan Dimethanol Diacrylate (TCDDMDA) was supplied by Arkema (Colombes, FR). Trimethylolpropane Trimethacrylate (TMPTMA), Isobornyl Methacrylate (IBOMA) and Bisphenol A Glycidyl Dimethacrylate (BisGMA) were obtained from Merck (Darmstadt, GER). The photoinitiator Bis-Acylphosphine Oxide (BAPO) was purchased from Sigma Aldrich (Steinheim, GER). While IBOMA and TCDDMDA act as reactive diluents to facilitate processing, BisGMA and TMPTMA act as oligomers to improve thermomechanical properties. BAPO acts as a photoinitiator. BisGMA and TCDDMDA have two functional groups; IBOMA one; and TMPTMA three.

For the cyanate ester (CE) part, Bisphenol E Dicyanate Ester (BECy, Primaset LECy), Primaset LVT50, and Primaset LVT100 were kindly provided by Arxada (Basel, CH). LVT50 is a blend of Bisphenol A Dicyanate Ester (BADCy) and a polyphenol cyanate resin, while LVT100 is a blend of BECy and a polyphenol cyanate resin. The mixing ratios are not specified by the manufacturer. For ease of reference, we will refer to the CEs only as BECy, LVT50, and LVT100. To prepare the catalyst for thermal curing, Copper Acetylacetonate was mixed with Nonylphenol, both purchased from Sigma Aldrich (Steinheim, DE).

## 2.2 | Resin Formulation and Curing

In the first step, Copper Acetylacetonate is stirred into nolyphenol in a ratio of 1:30 for 2 ± 0.1 h at 80°C ± 2°C. This mixture is then weighed with reference to the amount of CE to be used at 500 ppm (parts per million). The individual AY components are then weighed as shown in Table 1. BisGMA is first heated at 80°C ± 2°C for 20 ± 1 min to reduce its viscosity to a processable level. Once heated, BisGMA can be added, followed by the remaining components. The mixture is placed in an oven at 80°C ± 2°C for 20 ± 1 min and then stirred manually with a wooden spatula for 20 ± 1 s to allow the mixture to begin initial dissolution. The acrylate component is then returned to the oven at 80°C ± 2°C for 20 ± 1 min. This is followed by another manual mixing for 20 ± 1 s with the wooden spatula, followed by homogenization in a high speed mixer (Hauschild, Hamm, GER) at 2000 ± 10 rpm (revolutions per minute) for 2 ± 0 min.

Next, the CEs are prepared. For all three materials used, individual components crystallize over time (in the case of LVT100 and BECy) or completely crystallize after the first contact with air at room temperature (in the case of LVT50). Therefore, the required amount of CE is heated at 70°C ± 2°C for 1 ± 0 h and then homogenized for 30 ± 0 s at 2000 ± 10 rpm in a speed mixer. In case of unwanted recrystallization (for LVT50), the process must be repeated several times. The nomenclature of the samples is as follows: 20%BECy, for example, represents a total of 20% by weight of CE (BECy) and 80% by weight of AY. Table 2 shows the series of mixtures prepared in this work. "X" stands for a prepared mixture, while "-" symbolizes that no mixture has been prepared. Due to rapid recrystallization of LVT50 and partially overnight gelation of the AY-part when mixing BECy and AY above 50% CE content, the LVT50 and BECy series could not go to higher CE weight percentages because these conditions are unfavorable for resin printing.

UV post-curing of the components is performed on the multipurpose specimens for bending and notched bar impact tests and on the TGA specimens in the Nexa3D xCure (Ventura, USA) at a measured light intensity 27 ± 0.1 mW cm$^{-2}$ for 1 ± 0 h (total $E_{total}$ = 97.2 J cm$^{-2}$). This UV cabinet allows components to be cured uniformly from all sides in a single step. The DMA specimens were cured in the Prograprint Cure from Ivoclar (Schaan, LIE). Because of the one-sided curing, each side is first exposed to 8 ± 0.1 mW cm$^{-2}$ for 5 min and the same procedure is repeated for the other side. Then both sides are irradiated with 134 ± 0.5 mW cm$^{-2}$ for 1 min ($E_{total}$ = 20.8 J cm$^{-2}$). The samples with BECy and LVT50 were isothermally post cured at 150°C ± 2°C for 2 ± 0 h, the samples with LVT100 were isothermally post cured at 180°C ± 2°C for 2 ± 0 h. All samples had a long heating and cooling time of 12 h to prevent cracking during IPN formation.

## 2.3 | Material Characterization

### 2.3.1 | Photorheology

To determine the viscosity and the curing parameters, a photorheometer was used as described by Gorsche et al. [34] and shown schematically in Figure 2a. The photorheometer is a plate–plate design. The MCR 302 photorheometer used in this work is manufactured by Anton Paar (Graz, AUT). The stamp with a diameter of 12 ± 0.1 mm (PP12) is made of aluminum. The UV light source used is the SkyBeam system from Uvitron at a peak wavelength of 405 nm. The lower plate consists of a

**TABLE 1** | Resin composition for AY.

| Full name | Abbreviation | CAS-Number | Wt.% |
|---|---|---|---|
| Bisphenol A Glycidyl dimethacrylate | BisGMA | 1565-49-2 | 39.6 |
| Trimethylolpropane trimethacrylate | TMPTMA | 2390-92-4 | 39.6 |
| Isobornyl methacrylate | IBOMA | 7534-94-3 | 9.9 |
| Tricyclodecane dimethanol diacrylate | TCDDMDA | 42,594–17-2 | 9.9 |
| Bis-acyl phosphine oxide | BAPO | 162,881–26-7 | 1.0 |

**TABLE 2** | Mixture series.

| | 20 wt.% | 30 wt.% | 40 wt.% | 50 wt.% | 60 wt.% | 70 wt.% | 80 wt.% |
|---|---|---|---|---|---|---|---|
| BECy | X | X | X | X | — | — | — |
| LVT50 | X | X | X | X | — | — | — |
| LVT100 | X | X | X | X | X | X | X |

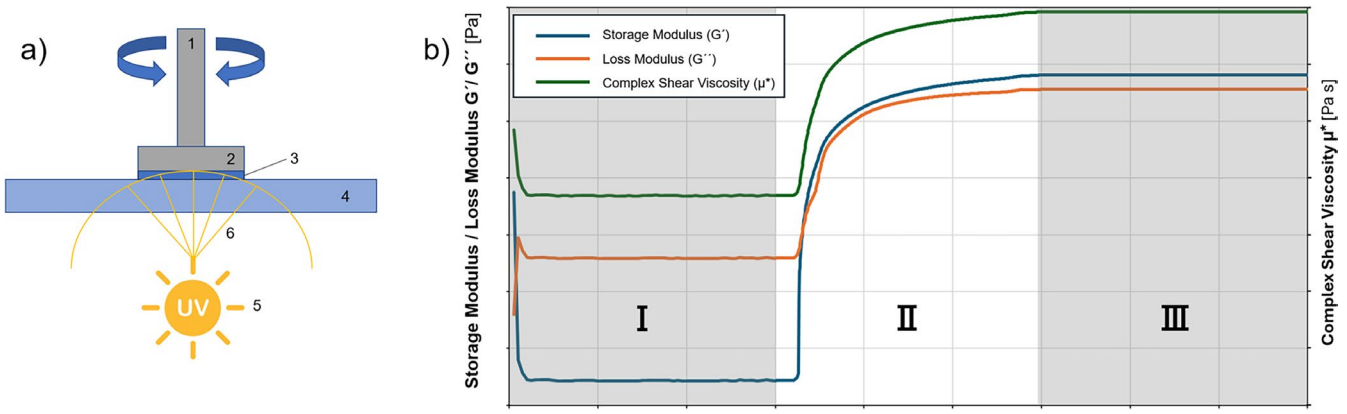


**FIGURE 2** | (a) Structure of the photorheometer. 1: Measuring tool, 2: Rheometer stamp, 3: Resin, 4: Glass plate, 5: UV source, and 6: UV rays; (b) Schematic phases of the photorheology. [Color figure can be viewed at wileyonlinelibrary.com]

UV-transparent glass layer. The resin sample in the measuring gap is irradiated by the UV lamp under the glass plate to measure the curing behavior, while the upper die attached to the tool measures the forces and torques that occur. The crosslinking shown via the intersection of the storage modulus ($G'$) and loss modulus ($G'$) is evaluated with the associated software RheoCompass of the connected PC. Since the UV light intensity should ideally correspond to the light intensity used later, the light source is adjusted so that it emits $3.9 \pm 0.1\,\mathrm{mW\,cm^{-2}}$. This is the best adjustable value for the measured output of the resin printer used later, the Elegoo Mars 2 Pro ($3.7 \pm 0.1\,\mathrm{mW\,cm^{-2}}$), a widely used DLP printer. To determine the light intensity, the UV meter LED F3 from Hönle (Gräfelfing, GER) is used, which outputs the measured values directly in mW $\mathrm{cm^{-2}}$. Before irradiating the samples, the complex shear viscosity $\mu^*$ was determined at a gap distance of 200 µm. An oscillating deformation of 1% and a frequency of 1 Hz was applied for 60 s. One measurement point per second was generated, and both the average and standard deviation were taken from the period 10 to 60 s to give the system enough time to settle. This first measurement step is visualized in Figure 2b with Phase I. The measurement of crosslinking under the influence of UV light started after these 60 s in Phase II. The UV source is switched on and the gelation point of the system is determined using the loss factor $tan\,\delta = 1$. These measurements were made at constant gap distances of 100, 200 and 300 µm. The following procedure can be used to calculate the working curve of the resin with its characteristic values of three measurements according to Jacobs et al. [35] In the first step, the time to gelation $t_{gel}$ is multiplied by the radiation intensity $3.9\,\mathrm{mW\,cm^{-2}}$ in order to calculate the total energy for gelation ($E_{max}$) of the system. The gap distances and the logarithmic values of $E_{max}$ are then plotted against each other. A straight line can be extrapolated from the points, for which the intersection with the x-axis is calculated.

The critical energy and penetration depth of UV light can be calculated using Equations (1) and (2). Here $E_{max}$ is the product of the radiation power and the exposure time, $E_c$ is the critical energy for gelation a resin, $D_p$ is the UV penetration depth of the light and $D_c$ is the height of the cured layer. The gap distances 100, 200 and 300 µm are then used for $D_c$. An average value with standard deviation can be calculated from the three $D_p$ values. The end of phase II can be used to measure the maximum storage modulus $G'$ and indicates the strength of the green body, while the maximum normal force $F_n$ is an indicator of shrinkage during UV curing [34]. For this reason the single measurements of $G'$ for a gap distance of 200 µm have been recorded, representing the actual maximum of DLP layer thickness. Phase III consists of a further irradiation and has the main purpose of facilitating the removal of the stamp from the glass plate after the measurement. Using the photorheometer characteristics, the optimum exposure times for DLP printing can be determined by conversion.

$$D_p = \frac{D_c}{\ln\left(\frac{E_{max}}{E_c}\right)} \tag{1}$$

$$E_c = e^{crossing\ point\ x-axis} \tag{2}$$

### 2.3.2 | Thermogravimetric Analysis (TGA)

The analysis of the fully cured samples in the TGA provides an insight into their thermal stability. The analysis was carried out on the TG 209 F1 Libra from Netzsch (Selb, GER) at a heating ramp of 10 K/min and a temperature range of 25°C–800°C. The measurement was performed in a synthetic air atmosphere with a flow rate of $250\,\mathrm{mL\,min^{-1}}$. The temperatures at which 5% relative mass loss ($T_{\Delta 5\%}$) occurs are determined as characteristic values. Three samples were tested per formulation, and the mean value with its standard deviation is provided.

### 2.3.3 | Dynamic Mechanical Analysis (DMA)

Dynamic mechanical analysis can be used to study the mechanical behavior of materials at different temperatures. $T_g$ was determined using dynamic mechanical analysis (DMA) in shear mode under oscillatory loading conditions. Three specimens, each measuring $50 \times 10 \times 2\,\mathrm{mm^3}$ with tolerances of $0.5 \times 0.2 \times 0.05\,\mathrm{mm^3}$, were tested. Measurements were performed with an oscillatory deformation of 0.1% at a frequency of 1 Hz while the temperature was increased from 25°C to 300°C at a controlled heating rate of $3\,\mathrm{K\,min^{-1}}$. A Rheometric Scientific RDA III from TA Instruments (New Castle, USA) was used for these tests. During the analysis, both the storage modulus $G'$

and the loss modulus $G''$ were recorded. $G'$ represents the elastic behavior of the material, indicating its ability to store energy and recover its original shape after deformation. $G''$ characterizes the viscous behavior of the material, where applied energy is dissipated rather than elastically stored. This dissipation is due to the viscoelastic nature of the material, which is influenced by molecular relaxation processes at elevated temperatures. The ratio of $G''$ to $G'$, called the loss factor $tan\ \delta$, peaks at $T_g$, indicating the transition point of the material (see Equation (3)). Peak broadening of the loss factor suggests a more complex IPN with partial phase separations [36]. The narrower the peak, the more homogeneous the structure of the network without phase separations and the smaller the glass transition region [37].

$$\tan \delta = \frac{G''}{G'} \tag{3}$$

During sample preparation, self-made steel molds measuring $50 \times 10 \times 2\,mm^3$ with tolerances of $0.5 \times 0.2 \times 0.05\,mm^3$ are first coated with UV release agent. The molds are then clamped onto the corresponding bases, and an additional layer of Teflon foil is inserted to close the gap between the mold and the base. In the next step, the resins are homogeneously heated to 40°C ± 2°C for 30 ± 2 min to reduce the viscosity for processing. Plastic pipettes are used to fill the molds bubble-free, and UV curing is performed. The specimens are then thermally cured and ground flat for finishing on the RotoPol-21 polishing and grinding machine (Willich, GER) with a force of 5 N and P80 SiC grinding wheels at 150 rpm in counter-rotation. To secure the specimens, double-sided adhesive tape is applied to a smoothing specimen holder to which the DMA samples are attached. The grinding time is variable, as grinding is continued until all samples have a smooth surface and the target thickness of 2 ± 0.05 mm is reached. Due to recrystallization and homogenization problems, no LVT50 samples could be analyzed; only BECy and LVT100 samples.

#### 2.3.4 | DLP

DLP printing for the multipurpose samples was performed using the Elegoo Mars 2 Pro (Shenzhen, CHN). This device has a measured luminous intensity of $3.7 \pm 0.1\,mW\,cm^{-2}$. The Chitubox program from CBT-Tech (Shenzhen, CHN) is used as the slicing software. The parts are then carefully removed from the printing platform with a metal spatula and washed with isopropanol in the Form Wash from Formlabs (Berlin, GER). The constant and variable printing parameters are listed in Table 3. The exposure time was calculated from the photorheology results.

#### 2.3.5 | Three-Point Bending

To evaluate the flexural strength ($\sigma_f$), flexural modulus ($E_f$) and maximum deflection to fracture ($\varepsilon_f$), five standardized $80 \times 10 \times 4\,mm^3$ multi-purpose specimens with tolerances of $1.0 \times 0.1 \times 0.1\,mm^3$ are printed in accordance with ASTM D790 and cured using UV light and thermal post-treatment. The specimens are then manually ground on the RotoPol-21 to remove burrs and other protrusions. The tests are carried out on the zwickiLine 2.5 from ZwickRoell (Ulm, GER).

**TABLE 3** | Parameters for DLP printing.

| Parameter | Value |
|---|---|
| Layer height | 50 µm |
| Lifting distance | 6 mm |
| Bottom layer count | 5 |
| Lifting speed | 80 mm/min |
| Exposure time | Variable |
| Bottom exposure time | 25 s |

#### 2.3.6 | Impact Strength (Charpy)

The notched impact strength $\alpha$ is tested in accordance with the standard for instrumented impact strength testing from DIN EN ISO 179-2. A sample set consists of five samples that conform to the standard. These samples are tested using the notched Charpy test on the RKP 5114 from ZwickRoell (Ulm, GER) with an impact energy of 50 ± 0 J. The same universal test specimens are used for the tests as for the bending tests and are finished in the same way ($80 \times 10 \times 4\,mm^3$ with tolerances of $1.0 \times 0.1 \times 0.1\,mm^3$). The lateral A-notch depth is 2 ± 0.2 mm. The specimens are tested parallel to the layers, which allows the layer adhesion to be examined more specifically.

#### 2.3.7 | Microscopy

To relate the results of $D_p$ to the actual print quality, small lattice cubes in the size of $21 \times 21 \times 21\,mm^3$ have been produced with selected formulations. The preview in the slicing program and one final result can be seen in Figure 3. To determine the difference between the target and actual geometry, the web width was measured using the Keyence VR 5000 (Osaka, JPN).

## 3 | Results and Discussion

### 3.1 | Photorheology

The viscosity of the three mixtures with the cyanate esters BECy, LVT50, and LVT100 decreases with increasing CE content (see Figure 4a). A higher proportion of low-viscosity cyanate ester is therefore advantageous for processability on a DLP printer, which has the typical viscosity limit of 3000 mPas and takes advantage of lower viscosity [38, 39]. The differences for the various viscosities can be explained by the molecular weights of the cyanate esters. LVT50 is a mixture of BADCy and a polyphenol cyanate ester, whereas LVT100 is a mixture of BECy and a polyphenol cyanate ester. The molecular weight of BECy is $250.25\,g\,mol^{-1}$ and of BADCy $278.31\,g\,mol^{-1}$, that is, due to its lower molecular weight, BECy has a lower viscosity than BADCy and therefore formulations with LVT100 also have a lower viscosity than formulations with LVT50. The $E_c$ curve in Figure 4b is identical for all three cyanate esters. As the amount of cyanate ester increases, the amount of UV-curable acrylate is reduced and therefore more energy is required to gelate the resin mixture. At 50% CE content, BECy, LVT50, and LVT100 are in the range of $19\,mJ\,cm^{-2}$.

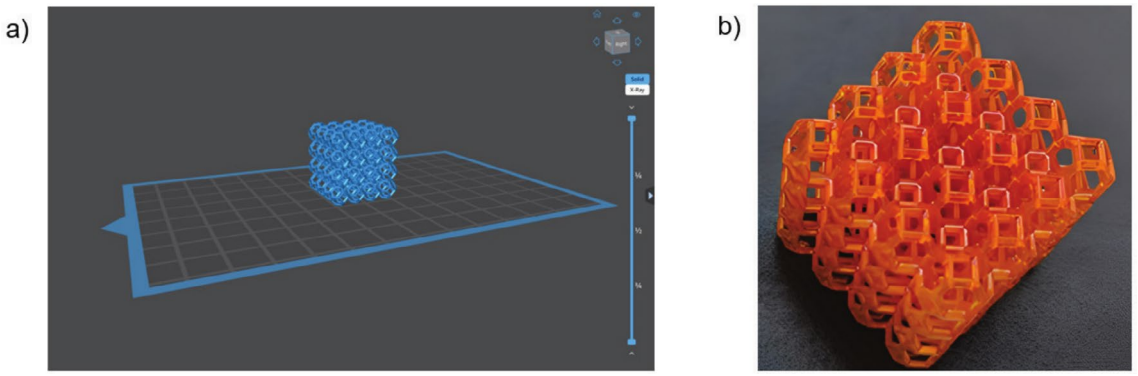


**FIGURE 3** | (A) Lattice cube in slicer; (b) Lattice cube 50% LVT100 after complete curing. [Color figure can be viewed at wileyonlinelibrary.com]

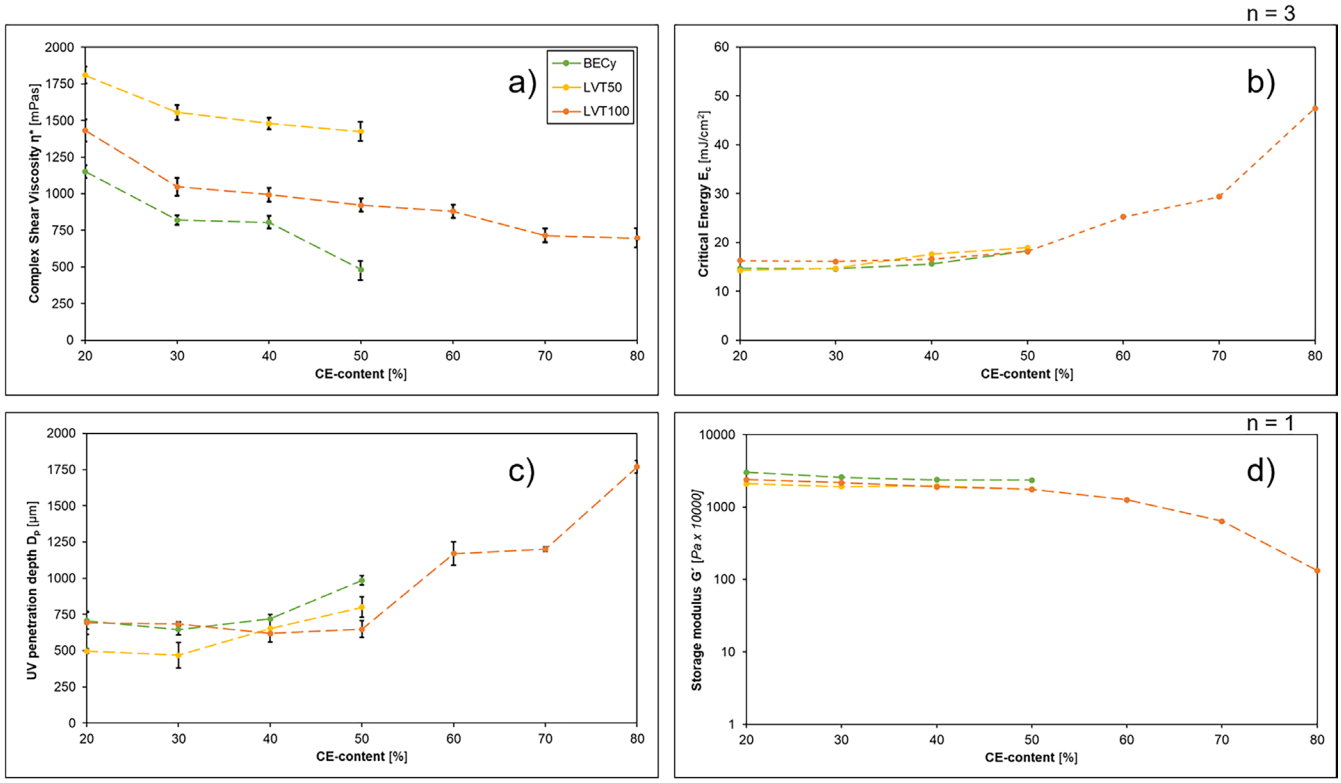


**FIGURE 4** | Results of photorheology. [Color figure can be viewed at wileyonlinelibrary.com]

Further increase of LVT100 leads to a sharp increase in $E_c$, indicating that processability on DLP can only be achieved with a strong light source or longer exposure times. $D_p$ follows the $E_c$ curves and tends to increase with the amount of CE, as shown in Figure 4c). This can be explained by the decreasing proportion of AY. Less acrylate also means fewer photoinitiators in the mixture, which statistically means that the UV rays travel a longer distance to reach a BAPO molecule, where they are absorbed and induce curing. From a CE content of 60%, the increases in $D_p$ are more pronounced due to further dilution of the photoreactive components, indicating that the level of detail for printing is compromised here. In Figure 4d), all resin blends show a clear trend of decrease of $G'$ with increasing CE content, especially from 60% CE content. $G'$ is an indicator of the green strength. The green strength reducing influence of a high CE content in the photorheometer is related to the cyanate ester which is still uncrosslinked and thus acts as a disruptive factor in the acrylate network [26]. At the same time, the values for $F_n$ drop more sharply at a CE content higher than 60% (see Table 4), which also indicates that UV curing plays a minor role from this formulation level onward.

## 3.2 | Thermogravimetric Analysis (TGA)

Figure 5a) shows the $T_{\Delta 5\%}$ values. A higher CE-content gradually allows for a higher thermal resistance because cyanate esters possess a higher decomposition temperature than acrylates [26]. Pure AY has a $T_{\Delta 5\%}$ of 325°C, while all cyanate esters have a $T_{\Delta 5\%}$ in the range of 400°C. With 50% CE content, LVT50 and LVT100 show the best properties. At 363°C, 50%BECy is about 7°C lower than the other two. The improved thermal resistance of LVT50 and LVT100 can be explained structurally by the incorporation of more aromatic compounds

**TABLE 4** | All values obtained from photorheology.

| Resin mixture | $\eta^*$ [mPa*s] | $G'$ [Pa] | $F_n$/N | $E_c$ [mJ/cm$^2$] | $D_p$ [μm] |
|---|---|---|---|---|---|
| 20%BECy | 1152 ± 46 | 3.03E+07 | 14.2 | 14.7 | 707 ± 57 |
| 30%BECy | 820 ± 44 | 2.58E+07 | 14.4 | 14.6 | 647 ± 38 |
| 40%BECy | 805 ± 33 | 2.37E+07 | 14.2 | 15.6 | 720 ± 7 |
| 50%BECy | 483 ± 43 | 2.36E+07 | 13.2 | 18.4 | 985 ± 32 |
| 20%LVT50 | 1810 ± 39 | 2.11E+07 | 12.7 | 14.3 | 497 ± 17 |
| 30%LVT50 | 1555 ± 58 | 1.92E+07 | 12.6 | 14.7 | 469 ± 88 |
| 40%LVT50 | 1480 ± 50 | 1.96E+07 | 9.2 | 17.6 | 654 ± 94 |
| 50%LVT50 | 1425 ± 40 | 1.76E+07 | 11.2 | 18.9 | 801 ± 70 |
| 20%LVT100 | 1433 ± 35 | 2.39E+07 | 13.6 | 16.3 | 693 ± 78 |
| 30%LVT100 | 1047 ± 75 | 2.17E+07 | 12.7 | 16.1 | 685 ± 15 |
| 40%LVT100 | 993 ± 60 | 1.91E+07 | 11.8 | 16.6 | 620 ± 5 |
| 50%LVT100 | 921 ± 47 | 1.75E+07 | 10.6 | 18.2 | 648 ± 57 |
| 60%LVT100 | 880 ± 45 | 1.26E+07 | 9.5 | 25.3 | 1171 ± 80 |
| 70%LVT100 | 715 ± 44 | 6.40E+06 | 7.3 | 29.4 | 1201 ± 16 |
| 80%LVT100 | 696 ± 46 | 1.33E+06 | 3.7 | 47.5 | 1769 ± 43 |

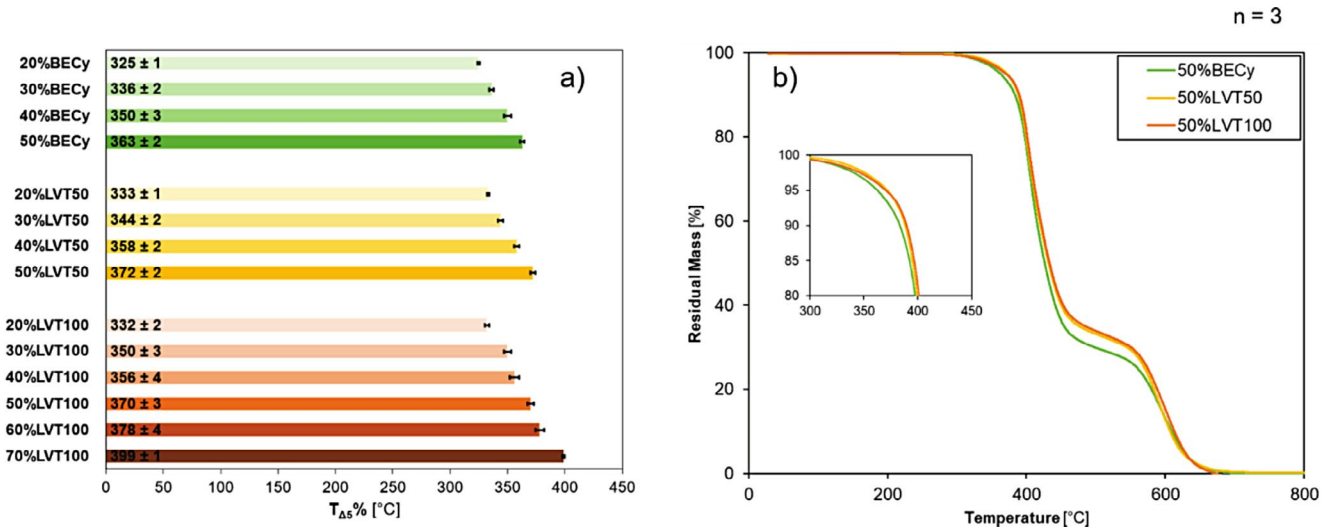


**FIGURE 5** | (a) $T_{\Delta 5\%}$ results from TGA; (b) Representative TGA curves for formulations with 50% CE content. [Color figure can be viewed at wileyonlinelibrary.com]

derived from the polyphenol cyanate component. To illustrate the overall curves, the formulations with 50% CE-content are compared with each other in Figure 5b). The resin systems degrade in two stages, with the acrylate component degrading first and the cyanate ester component degrading second. In the 450°C–550°C range, the mass loss of 50%BECy is about 5% higher than for the other resins. Thi s is due to the lower number of high temperature resistant aromatic compounds compared to the other resin blends. All resin blends decompose completely up to 800°C with no residual mass. The curves of 50%LVT50 and 50%LVT100 are almost congruent. This indicates that the structural composition is almost identical. The only difference is the use of the cyanate esters of BACy and BECy, which are chemically similar.

### 3.3 | Dynamic Mechanical Analysis (DMA)

To evaluate the DMA measurements, *tan δ* is plotted against the temperature. A single peak indicates a homogeneous interpenetrating polymer network (IPN) with a distinct glass transition temperature, suggesting mixing of the components at the molecular level. In contrast, two separate peaks indicate phase separation between the acrylate and cyanate ester components.

In some samples, no clear peak is visible, indicating a transition from a fully homogeneous IPN to a partially phase-separated IPN. This results in a broad overlapping peak rather than two distinct transitions [36]. In such cases, graphically modeled curves are placed in the plot in order to divide the broad single peak of the entire course into two individual peaks. Figure 6 illustrates this procedure using the curve of 40%BECy as an example. The AY component of the curve can thus be determined at 204°C and that of the CE component at 237°C.

The influence of a higher CE content on the *tan δ* curve becomes clear when looking at all the measurement curves (see Figure 7). On the one hand, the $T_g$ increases due to a higher CE content, and on the other hand, the resin blends start to form IPNs with partial phase separation from a certain amount of cyanate ester. For BECy, this occurs from 40% CE, and for LVT100, from 50% CE. In the course of the *tan δ*, this can be recognized by a clear broadening of the single peak with the formation of two shoulder peaks. Above this value, the two networks interfere with each other and show separate material properties. In conclusion, BECy can be used to obtain a homogeneous IPN up to a CE content of 40%, while LVT100 can be used to increase the CE content to 50%. The values in Table 5 also correspond to the $T_{\Delta 5\%}$ results, as LVT100 also shows superior properties compared to BECy due to the higher amount of aromatic compounds. This change in formulation also seems to have advantages in creating a homogeneous IPN. To the best of our knowledge, there could be several effects, such as the favorable π–π interactions between the aromatic compounds of BisGMA and LVT100, or better miscibility between the individual components of AY and LVT100, which induce this effect. Nevertheless, this effect needs to be further investigated in future publications.

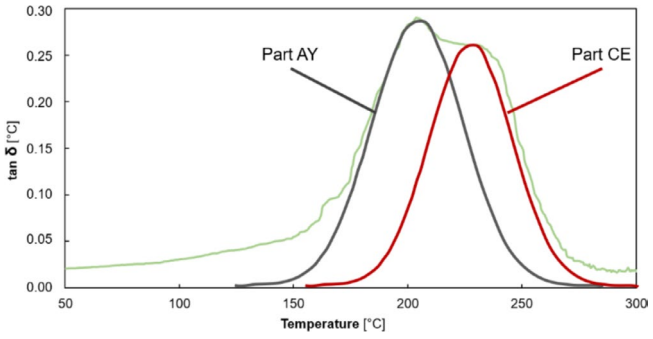


**FIGURE 6** | Determination of the individual *tan δ* curves with overlapping curves. [Color figure can be viewed at wileyonlinelibrary.com]

## 3.4 | DLP

From the photorheology results, it was extrapolated that the resin systems with 50% LVT100 should require an exposure time of 33 s. However, after the first print test, it was found that this value was too high, resulting in blurred details (see Figure 8). Further printing trials iteratively resulted in an optimum exposure time of 12 s. For this reason, the factor of 0.65 s/mJ cm$^{-2}$ was used to calculate the other prints of 50%BECy and 60%LVT100. For mechanical properties, samples were printed for 50%LVT100 and 50%BECy. The exposure times for 50%BECy and 50%LVT100 were 12 s, and for 60%LVT100 16 s (due to the higher $E_c$). To analyze the effect of $D_p$, two sets of lattice cubes were printed, one with 50%LVT100 and one with 60%LVT100.

## 3.5 | Three-Point Bending

In order to select the appropriate orientation for printing the multi-purpose samples, two orientations (x/y and z) were tested

**TABLE 5** | $T_g$ resulting from DMA.

| Resin mixture | $T_g$ Part AY [°C] | $T_g$ Single Peak [°C] | $T_g$ Part CE [°C] |
|---|---|---|---|
| 20%BECy | — | 198 ± 2 | — |
| 30%BECy | — | 199 ± 1 | — |
| 40%BECy | 206 ± 1 | — | 237 ± 1 |
| 50%BECy | 199 ± 1 | — | 253 ± 2 |
| 20%LVT100 | — | 208 ± 1 | — |
| 30%LVT100 | — | 220 ± 2 | — |
| 40%LVT100 | — | 235 ± 1 | — |
| 50%LVT100 | 227 ± 2 | — | 263 ± 1 |
| 60%LVT100 | 234 ± 1 | — | 274 ± 1 |
| 70%LVT100 | 230 ± 2 | — | 283 ± 1 |

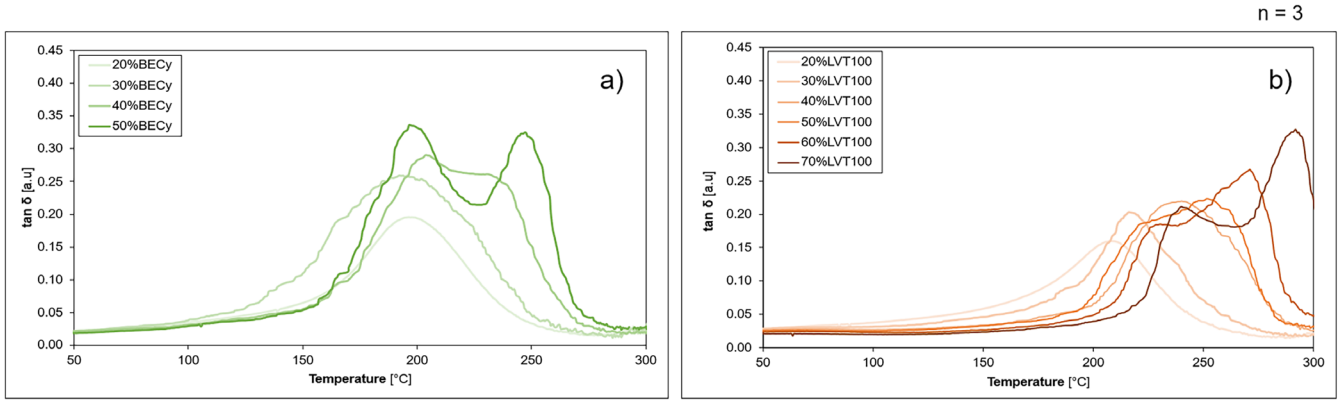


**FIGURE 7** | tan δ of the DMA measurements: (a) BECy systems and b) LVT100 systems. [Color figure can be viewed at wileyonlinelibrary.com]

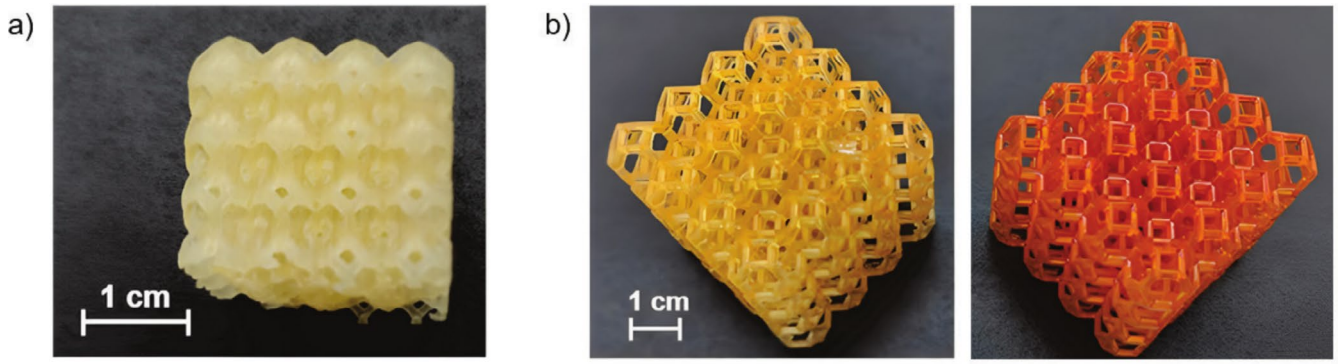


**FIGURE 8** | First printing trials a) Lattice cube 50% LVT100 with 33 s exposure time; b) Lattice cube 50% LVT100 with 12 s exposure time before thermal curing (left) and after thermal curing (right). [Color figure can be viewed at wileyonlinelibrary.com]

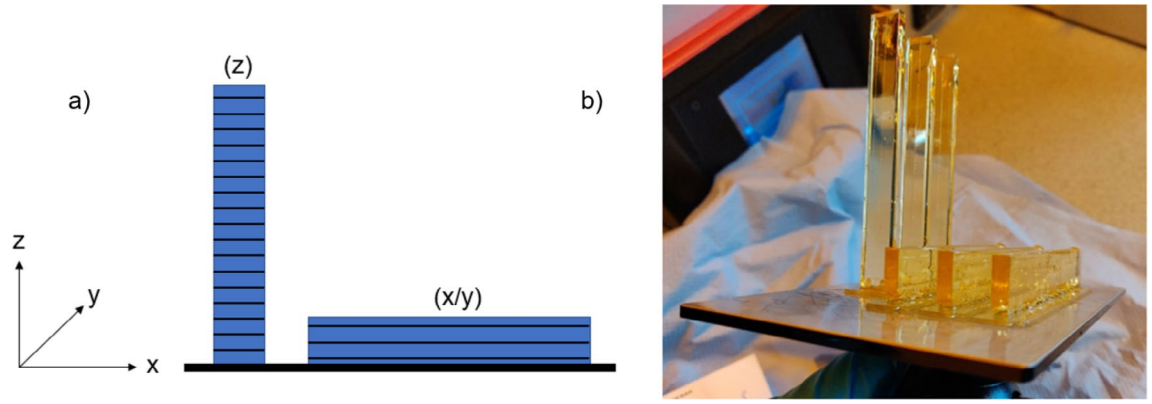


**FIGURE 9** | Different printing orientations. [Color figure can be viewed at wileyonlinelibrary.com]

**TABLE 6** | Results of the three-point bending tests and the Charpy tests; Results CE221 from technical data sheet [33]; *n*.s. = not specified; results with * are from tensile tests.

| Sample | Orientation | $E_f$ [GPa] | $\sigma_f$ [MPa] | $\varepsilon_f$ [%] | $\alpha$ [kJ m$^{-2}$] |
|---|---|---|---|---|---|
| 50%BECy | x/y | 3.5 ± 0.1 | 78.9 ± 5.3 | 2.2 ± 0.1 | — |
| 50%BECy | z | 3.7 ± 0.1 | 116.0 ± 13.8 | 3.1 ± 0.5 | 0.7 ± 0.0 |
| 50%LVT100 | z | 3.5 ± 0.1 | 116.0 ± 8.0 | 3.4 ± 0.3 | 0.8 ± 0.0 |
| CE221 | *n*.s. | 3.8 ± *n*.s. | 130.0 ± *n*.s. | 3.0 ± *n*.s.* | 1.2 ± 0.2 |

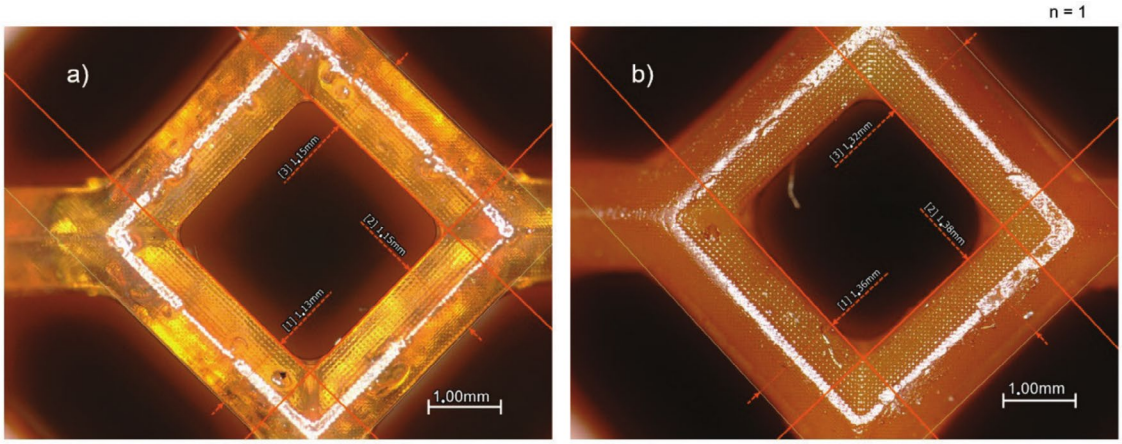


**FIGURE 10** | Micrsocopic picture of (a) 50%LVT100 and (b) 60%LVT100. [Color figure can be viewed at wileyonlinelibrary.com]

in preliminary trials at 50% BECy, as shown in Figure 9. The lines represent the schematic arrangement of the individual printing layers. The universal samples in x/y orientation are placed so that the narrow side touches the building platform, which facilitates removal from the platform after printing.

The exact results of the preliminary investigation are given in Table 6. In conclusion, it can be stated that the print in z-orientation does not show any differences in $E_f$ within the standard deviation compared to the x/y orientation, but has advantageous properties in terms of $\sigma_f$ and $\varepsilon_f$. A possible explanation could be the greater need for manual post-processing when grinding specimens in the x/y orientation. The specimens in the x/y direction have more support structures that need to be removed by grinding. This mechanical stress can introduce inconvenient microcracks during machining, which is why the universal specimens are generally manufactured in the z-direction. It is worth noting that the z-direction specimen often has the worst properties in other scientific work and is therefore an exception here for dual-cure resins. The interlayers are usually the weak points of printed parts due to the two intersecting polymerization interfaces, and a higher number of these (as in z-direction printing) means a higher probability of fracture at low stresses [40, 41].

To put the three-point bending results in context, we also included the only high-performance dual-cure DLP resin on the market, CE 221 by Carbon. This system is a combination of cyanate esters and acrylates, and its composition is not publicly available. Furthermore, its $T_g$ of 220°C is highly comparable to that of the systems presented here. The data in Table 6 are taken from the technical data sheet provided by the manufacturer. It was not possible to produce our own test specimens because the purchase and processing of the resin system is linked to the purchase of Carbon's high-priced CLIP printing technology and service program. In general, $E_f$, $\varepsilon_f$, and $\sigma_f$ are in the same range of mechanical properties as the commercial CE 221 system. The differences found between 50% BECy and 50% LVT100 are so small that they overlap within the limits of the comparatively small standard deviations. The curves of the flexure specimens are characterized by pure brittle and linear behavior. Considering only the mean values, $\sigma_f$ and $E_f$ of 50%BECy are slightly better than those of 50%LVT100. The elongation at break is identical for both resin blends. The mechanical values of the dual-cure printing resin CE 221 from Carbon are slightly higher than those of the resin blends tested here, which may be due to an optimization of the resin formulation with respect to mechanical properties on the part of Carbon. In addition, the printing parameters and orientations are not specified in the

**TABLE 7** | Overview of characterization methods and their key takeaways.

| Characterization method | Purpose in study | Key takeaways |
|---|---|---|
| Photorheology | Measure complex shear viscosity (μ*), critical gelation energy ($E_c$), and UV-penetration depth ($D_p$) during UV curing | Confirms that increasing CE-content reduces viscosity (improving DLP processability) but increases $E_c$ and $D_p$ and above 50 wt.% CE theoretically limiting printing resolution. |
| Thermogravimetric analysis (TGA) | Determine thermal stability via $T_{\Delta 5\%}$ | Shows increasing CE content enhances thermal stability. |
| Dynamic mechanical analysis (DMA) | Determine $T_g$ and network homogeneity via tan δ | Confirms homogeneous IPN formation up to 50 wt.% CE for LVT100 and 40 wt.% CE for BECy (single/narrow $T_g$ peak) Higher CE content causes phase separation (broadening/split peaks). |
| DLP printing trials | Evaluate practical printability and extrapolate curing settings out of the photorheology results with further sample preparation | Validates that practical curing settings can be extrapolated from to the photorheology results and ensures printability on low-entry DLP system compared to industrial solutions |
| Three-point bending | Measure $E_f$, $\sigma_f$, $\varepsilon_f$ for mechanical performance | Confirms that formulations containing 50 wt.% CE achieve comparable mechanical properties to an industrial resin. |
| Charpy impact test | Measure notched impact strength (α) | Indicates lower impact strength compared to an industrial resin, typical for high CE-content systems without tougheners |
| Microscopy | Analyze dimensional accuracy and detail resolution | Confirms accurate feature reproduction with 50 wt.% CE content of LVT100 while a CE content > 50 wt.% causes lower detail quality due to high $D_p$ |

CE221 data sheet, which means that the results vary greatly depending on the process settings.

### 3.6 | Impact Strength (Charpy)

While the differences between 50%BECy and 50%LVT100 are small, their behavior compared to carbon CE 221 is characterized by lower energy absorption in the Charpy test. Cyanate esters are particularly brittle, so it is possible that the lower $\alpha$ is due to a higher CE content compared to CE 221. Another possibility for the higher $\alpha$ of CE 221 is reinforcement with notched impact modifiers, which is not indicated in the technical data sheet [33]. However, this does not preclude the use of modifiers, as only substances that are potentially hazardous to health and the environment should be listed, and some commercially available modifiers such as rubber particles or other fillers are not covered by this risk assessment.

### 3.7 | Microscopy

To investigate the effect of $D_p$ on print quality, two different lattice cubes were compared (see Figure 10). While 50%LVT100 has a $D_p$ of 648 µm, 60%LVT100 has a $D_p$ of 1171 µm. The original web width in the stl. file is 1.25 mm. With a value of $1.14 \pm 0.01$ mm, the accuracy of 50%LVT100 is very high. The increased $D_p$ of 60%LVT100 results in a value of $1.35 \pm 0.03$ mm, which indicates a significant loss of detail quality. Therefore, it can be said that a $D_p$ of 1171 µm can be considered a critical limit above which prints may not be suitable for small geometries or fine details.

## 4 | Summary and Conclusion

In this work, we investigated how different amounts of cyanate ester affect the processability and final properties for dual-cure resin printing (DLP). There are several key takeaways from this work. First, a higher amount of CE significantly improved the thermal properties such as $T_g$ and $T_{\Delta 5\%}$. Nevertheless, it seems that the network starts to form heterogeneous IPNs with the use of CE above about 50 wt.%. When more CE is added, the viscosity of the systems is beneficially reduced, but the detail quality starts to lack at CE contents above 50 wt.% due to higher $E_c$ and $D_p$. In terms of mechanical properties, the systems presented here are almost on a par with the only commercially available system, CE 221. By demonstrating processability on a standard DLP printer, we have developed an open formulation that can be used and adapted by anyone. For example, the addition of flame retardants could further improve the use of, for example, 50% LVT100 by taking advantage of the high amount of CE, a polymer class that is itself flame retardant. The 50%LVT100 formulation shows the potential to be used even as a possible dual-use material due to the combination of excellent thermal and mechanical properties as well as good print quality on easily affordable DLP printers. Table 7 provides a quick overview of the key takeaways from the characterization techniques and how they are linked to the material and processing characteristics.

#### Author Contributions

**Max Friedel:** conceptualization (lead), data curation (lead), investigation (lead), methodology (lead), supervision (equal), validation (lead), visualization (lead), writing – original draft (lead). **Nico Geis:** investigation (supporting), methodology (equal). **Heiko Stieger:** methodology (equal). **Holger Ruckdaeschel:** funding acquisition (lead), project administration (lead), supervision (lead), writing – review and editing (lead).

#### Acknowledgments

We would like to thank all colleagues of the work group "Resins & Composites" at the Department of Polymer Engineering for their support. Open Access funding enabled and organized by Projekt DEAL.

#### Conflicts of Interest

The authors declare no conflicts of interest.

#### Data Availability Statement

The authors have nothing to report.

#### References

1. M. Maniruzzaman, *3D and 4D Printing in Biomedical Applications: Process Engineering and Additive Manufacturing* (John Wiley & Sons, 2018).

2. S. Hoskins, *3D Printing* (Bloomsbury Publishing Plc, 2018).

3. L. Gardner, "Metal Additive Manufacturing in Structural Engineering – Review, Advances, Opportunities and Outlook," *Structure* 47 (2023): 2178–2193.

4. N. Bauriedel, R. Q. Albuquerque, J. Utz, N. Geis, and H. Ruckdäschel, "Monitoring of Fused Filament Fabrication (FFF): An Infrared Imaging and Machine Learning Approach," *Journal of Polymer Science* 62 (2024): 5633–5641.

5. J. C. Vasco, *Additive Manufacturing* (Elsevier, 2021), 505–530.

6. J. C. Najmon, S. Raeisi, and A. Tovar, *Additive Manufacturing for the Aerospace Industry* (Elsevier, 2019), 7–31.

7. S. Singamneni, Y. Lv, A. Hewitt, R. Chalk, W. Thomas, and D. Jordison, "Additive Manufacturing for the Aircraft Industry: A Review," *Journal of Aeronautics & Aerospace Engineering* 8, no. 1 (2019).

8. S. Raja, R. M. Ali, Y. V. Babar, et al., "Integration of Nanomaterials in FDM for Enhanced Surface Properties: Optimized Manufacturing Approaches," *Applied Chemical Engineering* 7 (2024): 123–135.

9. D. P. Mohanty, B. J. Arnold, S. Baruah, S. Chandrasekar, and J. B. Mann, "A New Class of High Performance Metal-Fiber Thermoplastic Composites for Additive Manufacturing," *Composites Part A: Applied Science and Manufacturing* 169 (2023): 107519.

10. T. J. Hoskins, K. D. Dearn, and S. N. Kukureka, "Mechanical Performance of PEEK Produced by Additive Manufacturing," *Polymer Testing* 70 (2018): 511–519.

11. J. Utz, N. Geis, M. Baur, and H. Ruckdäschel, *5th International Conference on Current Scenario in Pure and Applied Mathematics (ICCSPAM-2022)* (AIP Publishing, 2023).

12. T. A. Lima, A. Fridman, J. McLaughlin, et al., "High Performance Thermosets for Additive Manufacturing," *Innovative Emergency Technologies* 10 (2023): 2330003.

13. M. Kalender, S. E. Kilic, S. Ersoy, Y. Bozkurt, and S. Salman, *2019 9th International Conference on Recent Advances in Space Technologies (RAST)* (IEEE, 2019), 689–694.

14. D. W. Martinez, M. T. Espino, H. M. Cascolan, J. L. Crisostomo, and J. R. C. Dizon, "A Comprehensive Review on the Application of 3D Printing In the Aerospace Industry," *Key Engineering Materials* 913 (2022): 27–34.

15. M. Pagac, J. Hajnys, Q.-P. Ma, et al., "A Review of Vat Photopolymerization Technology: Materials, Applications, Challenges, and Future Trends of 3D Printing," *Polymers* 13 (2021): 598.

16. O. Konuray, X. Fernández-Francos, X. Ramis, and À. Serra, "State of the Art in Dual-Curing Acrylate Systems," *Polymers* 10 (2018): 178.

17. R. Chaudhary, P. Fabbri, E. Leoni, F. Mazzanti, R. Akbari, and C. Antonini, "Additive Manufacturing by Digital Light Processing: A Review," *Progress in Additive Manufacturing* 8 (2023): 331–351.

18. L. Schittecatte, V. Geertsen, D. Bonamy, T. Nguyen, and P. Guenoun, "From Resin Formulation and Process Parameters to the Final Mechanical Properties of 3D Printed Acrylate Materials," *MRS Communications* 13 (2023): 357–377.

19. J. W. Stansbury, "Dental Materials: Official Publication of the Academy of Dental Materials," *Dental Materials* 28 (2012): 13–22.

20. I. Binyamin, E. Grossman, M. Gorodnitsky, D. Kam, and S. Magdassi, "3D Printing Thermally Stable High-Performance Polymers Based on a Dual Curing Mechanism," *Advanced Functional Materials* 33 (2023): 2214368.

21. Z. Chen, M. Yang, M. Ji, X. Kuang, H. J. Qi, and T. Wang, "Recyclable Thermosetting Polymers for Digital Light Processing 3D Printing," *Materials & Design* 197 (2021): 109189.

22. M. Romeis and D. Drummer, "A Dyciandiamine-Based Methacrylate-Epoxy Dual-Cure Blend-System for Stereolithography," *Polymers* 13 (2021): 3139.

23. B. Zhang, A. Serjouei, Y.-F. Zhang, et al., "Dual-Stage Thermosetting Photopolymers for Advanced Manufacturing," *Chemical Engineering Journal* 411 (2021): 128466.

24. I. Hamerton and S. Takeda, "A Study of the Polymerization of Novel Cyanate Ester/Acrylate Blends," *Polymer* 41 (2000): 1647–1656.

25. T. Wu, P. Jiang, Z. Ji, et al., "3D Printing of High-Performance Isocyanate Ester Thermosets," *Macromolecular Materials and Engineering* 305 (2020): 2000397.

26. Z.-X. Zhou, Y. Li, J. Zhong, et al., "High-Performance Cyanate Ester Resins With Interpenetration Networks for 3D Printing," *ACS Applied Materials & Interfaces* 12 (2020): 38682–38689.

27. Y. S. Lipatov and T. T. Alekseeva, "Phase-Separated Interpenetrating Polymer Networks," *Phase-Separated Interpenetrating Polymer Networks* 208 (2007): 1–227.

28. M. Shivashankar and B. K. Mandal, "A Review on Interpenetrating Polymer Network," *International Journal of Pharmacy and Pharmaceutical Sciences* 4 (2012): 1–7.

29. O. Konuray, J. M. Morancho, X. Fernández-Francos, M. García-Alvarez, and X. Ramis, "Curing Kinetics of Dually-Processed Acrylate-Epoxy 3D Printing Resins," *Thermochimica Acta* 701 (2021): 178963.

30. A. W. Bassett, A. E. Honnig, J. J. La Scala, and J. F. Stanzione, "Network Toughening of Additively Manufactured, High Glass Transition Temperature Materials via Sequentially Cured, Interpenetrating Polymers," *Polymer International* 70 (2021): 749–758.

31. R. J. Iredale, C. Ward, and I. Hamerton, "Modern Advances in Bismaleimide Resin Technology: A 21st Century Perspective on the Chemistry of Addition Polyimides," *Progress in Polymer Science* 69 (2017): 1–21.

32. C. Frank, C. Gorsche, and R. Gmeiner, "Resin Composition 2018–04–08." https://data.epo.org/publication-server/rest/v1.0/publication-dates/20220209/patents/EP3949731NWA1/document.pdf.

33. D. L. S. Carbon, "Technical Data Sheet-CE 221 Cyanatester." https://xometry.pro/wp-content/uploads/2023/07/CE-221-Cyanatester-1.pdf.

34. C. Gorsche, R. Harikrishna, S. Baudis, et al., "Real Time-NIR/MIR-Photorheology: A Versatile Tool for Thein Situ Characterization of Photopolymerization Reactions," *Analytical Chemistry* 89 (2017): 4958–4968.

35. P. F. Jacobs, *Rapid Prototyping & Manufacturing: Fundamentals of Stereolithography* (Society of Manufacturing Engineers, 1992).

36. J. Fan, X. Hu, and C. Y. Yue, "Static and Dynamic Mechanical Properties of Modified Bismaleimide and Cyanate Ester Interpenetrating Polymer Networks," *Journal of Applied Polymer Science* 88 (2003): 2000–2006.

37. S. Marinovic, I. Popovic, B. Dunjic, S. Tasic, B. Bozic, and D. Jovanovic, "The Influence of Different Components on Interpenetrating Polymer Network's (IPN'S) Characteristics as Automotive Top Coats," *Progress in Organic Coatings* 68 (2010): 293–298.

38. D. A. Komissarenko, P. S. Sokolov, A. D. Evstigneeva, I. A. Shmeleva, and A. E. Dosovitsky, "Rheological and Curing Behavior of Acrylate-Based Suspensions for the DLP 3D Printing of Complex Zirconia Parts," *Materials* 11 (2018): 2350.

39. A. Vyas, V. Garg, S. B. Ghosh, and S. Bandyopadhyay-Ghosh, "Photopolymerizable Resin-Based 3D Printed Biomedical Composites: Factors Affecting Resin Viscosity," *Materials Today Proceedings* 62 (2022): 1435–1439.

40. A. Keßler, R. Hickel, and N. Ilie, "In vitro Investigation of the Influence of Printing Direction on the Flexural Strength, Flexural Modulus and Fractographic Analysis of 3D-Printed Temporary Materials," *Dental Materials Journal* 40 (2021): 641–649.

41. Y. A. Al-Dulaijan, L. Alsulaimi, R. Alotaibi, et al., "Effect of Printing Orientation and Postcuring Time on the Flexural Strength of 3D-Printed Resins," *Journal of Prosthodontics* 32 (2023): 45–52.